Elastic Thickness Compressibilty of the Red Cell Membrane

Volkmar Heinrich,* Ken Ritchie,† Narla Mohandas,‡ and Evan Evans*§

*Department of Biomedical Engineering, Boston University, Boston, Massachusetts 02215, USA; †Department of Biological Science, University of Nagoya, Nagoya, Japan; ‡Life Sciences Division, Lawrence Berkeley Laboratory, Berkeley, California 94720, USA; and §Department of Physics and Astronomy, University of British Columbia, Vancouver, British Columbia V6T 2A6, Canada

ABSTRACT We have used an ultrasensitive force probe and optical interferometry to examine the thickness compressibility of the red cell membrane in situ. Pushed into the centers of washed-white red cell ghosts lying on a coverglass, the height of the microsphere-probe tip relative to its closest approach on the adjacent glass surface revealed the apparent material thickness, which began at ~90 nm per membrane upon detection of contact (force ~1–2 pN). With further impingement, the apparent thickness per membrane diminished over a soft compliant regime that spanned ~40 nm and stiffened on approach to ~50 nm under forces of ~100 pN. The same force-thickness response was obtained on recompression after retraction of the probe, which demonstrated elastic recoverability. Scaled by circumferences of the microspheres, the forces yielded energies of compression per area which exhibited an inverse distance dependence resembling that expected for flexible polymers. Attributed to the spectrin component of the membrane cytoskeleton, the energy density only reached one thermal energy unit (k_BT) per spectrin tetramer near maximum compression. Hence, we hypothesized that the soft compliant regime probed in the experiments represented the compressibility of the outer region of spectrin loops and that the stiff regime <50 nm was the response of a compact mesh of spectrin backed by a hardcore structure. To evaluate this hypothesis, we used a random flight theory for the entropic elasticity of polymer loops to model the spectrin network. We also examined the possibility that additional steric repulsion and apparent thickening could arise from membrane thermal-bending excitations. Fixing the energy scale to k_BT/spectrin tetramer, the combined elastic response of a network of ideal polymer loops plus the membrane steric interaction correlated well with the measured dependence of energy density on distance for a statistical segment length of ~5 nm for spectrin (i.e., free chain end-to-end length of ~29 nm) and a hardcore limit of ~30 nm for underlying structure.

INTRODUCTION

The red blood cell membrane is one of the most thoroughly researched structures in biology. The membrane material is a composite design based on a fluid lipid bilayer supported by a scaffolding of interconnected proteins and studded by a superficial forest of peptidoglycans. From micromechanical measurements (Mohandas and Evans, 1994), well defined elastic moduli for surface area dilation, shear, and bending have been shown to govern red cell deformability. Likewise, from electron microscopy (Byers and Branton, 1985; McGough and Josephs, 1990) and biochemical analysis (Bennett, 1990; Mohandas and Evans, 1994), a detailed model has been constructed of a beautifully triangulated network of flexible spectrin proteins plus its complex protein linkage to the bilayer. But even with this rich description of structure, composition, and mechanics, the picture is mainly a two-dimensional projection of the red cell membrane architecture and material properties. Little is known about how structural components are arrayed and interact in the third dimension normal to the membrane.

For more than two decades, red cell membrane structure in schematics has been portrayed as a thick lipid bilayer with a thin, flat mesh of attached proteins (Cohen, 1983; Bennett, 1990). A recent rendition (Picart and Discher, 1999; Fig. 1) shows a more realistically sparse-extended spectrin network tethered by junctional complexes of short actin filaments, globular band 4.1, and other proteins to glycophorin C in a thin lipid bilayer. Also depicted within this cross-section are large cytoplasmic-face ankyrin plus lipid-anchored band 3 proteins believed to interact with the spectrin network somewhere between the junctional complexes. Beyond the ~4 nm thick lipid bilayer, the exterior glycocalyx extends the bilayer foundation of the membrane to the order of ~10 nm in Fig. 1 as deduced from electron microscopy (Linss et al., 1991) and studies of electrophoretic mobility (Levine et al., 1983). Representing the foundation for nodes of the spectrin network, the junctional complexes separate the network from the lipid interface by ~10 nm. Finally, with values of contour length and network topology known to characterize the spectrin cytoskeleton, simulations of spectrin networks with different numbers of segments per chain (Boal, 1994) have indicated that the chains extend ~20–30 nm from the junctional complexes into the cytoplasm. Hence, from these estimates of compact molecular dimensions and simulations of polymer networks, a red cell membrane is expected to span ~40–50 nm in thickness and, if squeezed, to exhibit a structural hardness of ~20–25 nm.

To test this view of membrane structure in situ, we have used a biomembrane force probe (BFP; Evans et al., 1995) and optical interferometry to measure the double membrane

---

Received for publication 12 July 2000 and in final form 30 May 2001.

Address reprint requests to Dr. Evan A. Evans, University of British Columbia, Department of Physics and Pathology, 6224 Agricultural Road, Vancouver, BC V6T 2A6, Canada. Tel.: 604-822-7579; Fax: 604-822-7635; E-mail: evans@physics.ubc.ca.

0006-3495/01/09/1452/12 $2.00

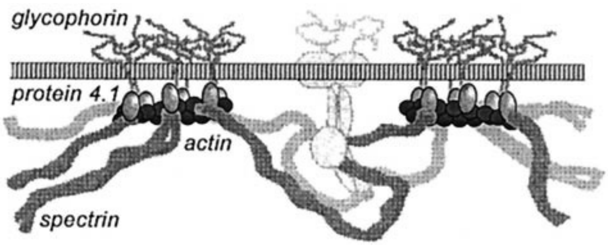

FIGURE 1 Schematic representation of red cell membrane architecture reproduced from Picart and Discher (1999) that depicts the lipid bilayer (*thin-lined slab*) studded with a superficial forest of glycoproteins and supported by a subsurface network of spectrin tetramers which is linked to the bilayer by actin/4.1 junctional complexes. Also depicted is a complex of band 3/ankyrin (*light gray*) putatively bound to spectrin between the junctional complexes.

thicknesses of washed-white red cell ghosts resting on a coverglass. The two membrane faces of a ghost were compressed by a ~4-μm spherical-glass BFP tip under repeated cycles of force from 0 to 100 pN. Reflection interference optics were used to encode the separation from the coverglass as a Newton-ring fringe pattern, which was monitored through video microscropy. Analyzed in real-video time (30 frames/s), the reflection interference image of the probe tip was converted to the distance from the coverglass with nanometer resolution. In each test, the probe was first touched to the coverglass beside the ghost to establish the reference height set by molecular-scale roughness on the substrates and then pushed into the center of the ghost to determine the thickness added by the two membranes. As expected, thickness of the red cell membrane decreased under compression to a limit where force rose very steeply but then recovered elastically to give the same force-thickness curve upon recompression. Relative to the closest approach to the adjacent glass surface and divided by two to represent a single membrane, the compliant regime covered a large distance from ~90 nm to ~50 nm, whereupon the membrane stiffened significantly. Attributing the origin of membrane compliance to the spectrin network, our method of analysis has been to correlate the force-thickness measurements with an ideal random flight theory for loops of polymer chains tethered to a surface backed by a rigid structure. Moreover, we have also examined the extent to which membrane thermal-bending undulations increase apparent thickness and extend elastic response through long-range steric interaction. Including the effect of thermal undulations, we obtain an excellent match of the idealized elastic model for polymer loops to the measurements of membrane compressibility over the full range of thickness which provides both a description of membrane geometry and properties of the spectrin network in the third dimension.

MATERIALS AND METHODS

Red cell ghosts

Red cells were separated by low speed centrifugation from whole blood samples. The isolated cells were washed three times in a sodium phosphate buffer (5 mM NaH_2PO_4-Na_2HPO_4 plus 150 mM NaCl, pH 8). To ghost the red cells, the sample was suspended in cold (4°C) lysis buffer (5 mM NaH_2PO_4-Na_2HPO_4, pH 8) for 5 min. The cold-lysis step was repeated two more times to produce white ghosts with minimal hemoglobin content. Then, low ionic strength buffer was added (5 mM NaH_2PO_4-Na_2HPO_4 plus 15 mM NaCl, pH 8) and the ghosts were allowed to reseal at 37°C for 10 min. For thickness tests, the ghosts were suspended in 150 mOsm of phosphate-buffered saline, pH 7.4, plus 1 mg/ml of serum albumin, which caused the ghosts to shrink to flattened disks. Because of the small ghost volume, the upper and lower membranes were flattened together over a large central region and the cytosol was relegated to a narrow annulus at the cell perimeter.

Glass microsphere probe tips

In preparation for attachment to the BFP transducer, polyethylene oxide PEG polymers with biotin end groups were covalently linked to glass microspheres by a procedure developed in our previous studies (Evans et al., 1995). Borosilicate microspheres (Duke Scientific, Palo Alto, CA) of ~4-μm diameter were chosen for probe tips. The microspheres were cleaned in a mixture of ammonium hydroxide, hydrogen peroxide, and water at boiling temperature, then washed several times in nanopure water. After cleaning, aminosilane groups (AEAPTMS, United Chemical Technologies, Bristol, PA) were attached to the microspheres and the spheres were baked in a clean drying oven to enhance covalent bonding. The aminosilanized microspheres were reacted with a mixture of heterobifunctional PEG-biotin polymers (NHS-PEG3400-biotin, Shearwater Polymers, Huntsville, AL). The microspheres were then saturated with streptavidin (Pierce Chemical Co., Rockford, IL) and washed before attachment to a biotinylated BFP capsule as described below.

Assembly and control of the BFP transducer

For use as BFP transducers, human red cells were isolated from fresh blood samples by low speed centrifugation. After washing, the transducer cells were covalently linked with PEG-biotin polymers also using the heterobifunctional amine reactive NHS-PEG3400-biotin (Shearwater Polymers). Once biotinylated, a red cell capsule and streptavidinated microsphere were selected from microchambers on the microscope stage by micromanipulation and maneuvered to form strong adhesive contact. Pressurized into a spherical shape by micropipette suction (aspiration pressure ΔP and pipette radius R_p), the red cell-microsphere assembly became the biomembrane force probe as seen in Fig. 2 (Evans et al., 1995). Directly proportional to membrane tension τ_m, the force constant k_f (force/capsule extension) was set by choosing the pipette suction as described by Evans et al. (1995),

$$k_f \approx 2\pi\,\tau_m/\log_e(4R_0^2/R_cR_p)$$
$$\tau_m = \Delta P\,R_p/2(1 - R_p/R_0) \qquad (1)$$

where R_0 is the radius of the outer-spherical cell region and R_c is the radius of membrane-bonded contact to the microsphere tip. The full span of the force constant is from 0.1 to 3 pN/nm but values of 0.2–0.6 pN/nm were used to test ghost membrane compressibility. Operated on the stage of a Zeiss Axiovert microscope (Carl Zeiss, Inc., Thornwood, NY) and demonstrated in Fig. 2, the BFP was translated along the optical axis to/from contact with the ghost or coverglass by precision-piezo control at speeds of ~30 nm/s. Zeiss Antiflex optics were used to encode the separation between the microsphere tip and coverglass surface in a Newton-ring

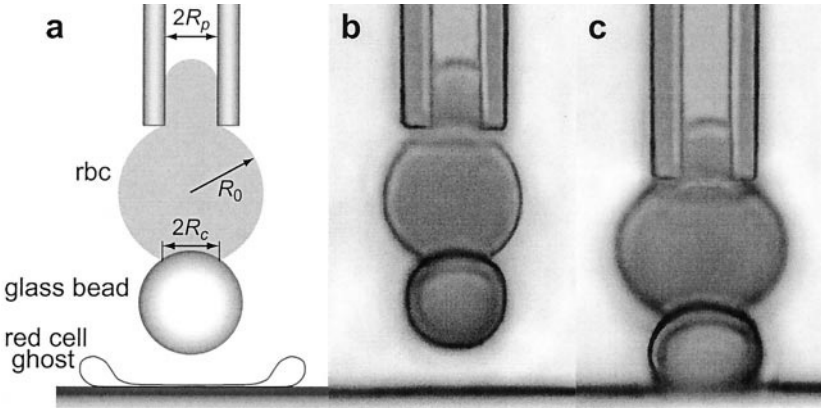

FIGURE 2 (*a*) Schematic of a biomembrane force probe BFP above a red cell ghost. (*b*, *c*) Viewed horizontally, video images demonstrate how the BFP with a ~4-μm glass microsphere tip was maneuvered close to, and pushed against, the glass substrate. Deflection (compression) Δz of the transducer capsule multiplied by the transducer *spring* constant k_f (~pipette suction × radius) revealed the compression force $f = k_f \Delta z$.

interference pattern (Fig. 3). Taking advantage of the flattened ghosts, we were able to use relatively large microspheres for probe tips without pressurizing the cytosol inside the ghost. The ~4-μm diameter spheres produced sufficient numbers of fringes in the Newton-ring patterns to enable nanometer resolution in microsphere-substrate separation. Through computer video-image analysis, the fringe pattern was converted to tip-surface distance at the contemporary rate of 30/s as described below. The difference between piezo translation and tip movement defined the transducer deflection which, multiplied by the force constant, specified the instantaneous axial force.

Reflection interference images and analysis of tip-surface distance

Reflection interference contrast microscopy was used to resolve the microsphere-coverglass separation at distances well below the wavelength of light. The Zeiss Antiflex optics included a 63×, 1.25 numerical aperture Plan-Neofluar oil immersion objective with integrated one-quarter–wave plate, reflector-slider with polarizer, analyzer, and dichroic mirror. With epi-illumination by an Oriel 100 W Hg arc lamp at 546.1 nm wavelength, a Newton-ring pattern was created by interference between light reflected from the coverslip-buffer interface and from the lower surface of the microsphere. Captured at 30 frames/s with a CCD-72 (Dage MTI, Inc., Michigan City, IN) video camera, the fringe pattern was digitized (Matrox Meteor-II 8 bit frame grabber) in a small window centered around the pattern. The magnification of the digitized image was ~72.4 nm/pixel. The center of the fringe pattern was located in real-video time by searching for the intersection of two perpendicular symmetry axes. From the centered pattern, a circularly averaged radial intensity profile was obtained to maximize signal-to-noise and was determined at radii increasing in half-pixel steps as shown in Fig. 3. The search box was then recentered around the interference pattern for the next time step.

Under precision-piezo translation of the probe, the microsphere was imaged over a large range of well defined displacements before touch. This enabled us to verify the accuracy of the analysis used to extract distances from the interference patterns and to accurately determine the microsphere radius. Although methods of reflection interference contrast microscopy analysis published in the literature have been improved (Wiegand et al., 1998), we found these descriptions either difficult to implement in real time or unable to accurately reproduce the calibrated piezo displacement of the 4-μm bead over the full range of distance. Hence, we carefully examined the factors governing image formation and established a reliable method to extract the full range of separation distances from the Newton-ring pattern.

As described in Appendix I, the key step is to set the position of focus and thereby fix the locus of the interference pattern imaged by the microscope. The fringe spacing can then be determined precisely as a function of separation distance, which is essential in the analysis. With Eq. AI-3 in Appendix I, the microsphere radius R_S was first determined from correlation of the intensity function to fringe patterns over a large range of heights above bare coverglass (Fig. 3 *a*). The efficacy of the height analysis was demonstrated by close agreement between the microsphere displacements obtained from the Newton-ring patterns and the piezo translation of the force probe over the large range of distance. Then, the distance from the coverglass with/without an intervening red cell ghost was found in each video frame using the value established for the microsphere radius. As demonstrated in Fig. 3 *b*, the red cell ghost had negligible affect on the Newton-ring image of the microsphere because the membranes contributed little to the integral of absolute index of refraction over the optical path. [Although difficult to specifiy accurately, the contribution of one membrane to the optical path length can be estimated by taking the differential optical thickness of a lipid bilayer (refractive index of ~1.5 minus 1.34 for the buffer × thickness of ~4 nm) and multiplying by the ratio of red cell membrane total mass to lipid mass (~100:40). This estimate yields a small fixed adjustment of ~−1.6 nm per membrane to the apparent separation.]

Conversion of probe force to elastic energy per area

After touch to the adjacent glass substrate for reference (Fig. 4 *a*), the probe was pushed into the ghost as illustrated in Fig. 4 *b*. Deviation between piezo translation of the probe and movement of the tip revealed the probe deflection, which thereby established the force of compression as a function of distance (Fig. 4 *c*). Given free slip at the interfaces, the force f applied with a large sphere (radius R_S) to compress a thin elastic material against a flat substrate is described by the integral of the axial stress σ_z (defined positive for tension) over the material contact, i.e.,

$$f \approx -2\pi R_S \int_{o\rightarrow\Delta z} \sigma_z \, dz$$

$2\pi\, R_S\, dz$ defines an annular element of area on the sphere in terms of the axial distance z, and the total contact area $2\pi R_S\, \Delta z$ is set by the indentation Δz. Because the material is very thin compared with the radius of the sphere and free to expand outward under compression, radial and transverse shear stresses can be neglected so that axial stress on each element of the material depends mainly on local thickness. Thus, the axial stress can be described by the derivative of the local energy density ϵ (per area) with respect to thickness,

$$\sigma_z = \partial\epsilon/\partial z \tag{2}$$

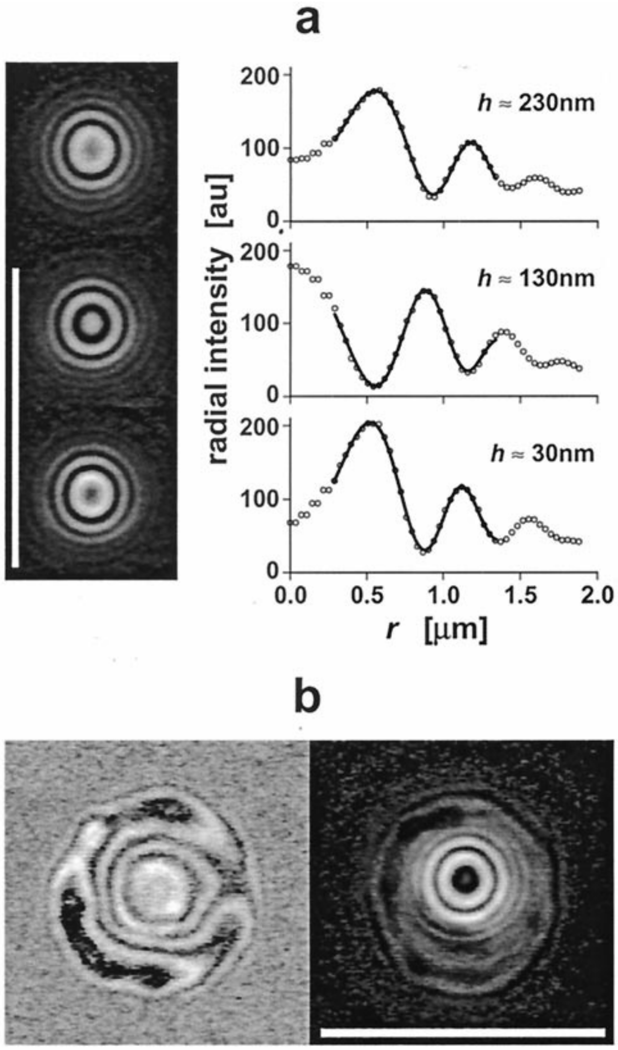

FIGURE 3 (*a*) Newton-ring interference patterns created by reflection interference from a ~4-μm diameter glass tip of the BFP above a bare coverglass (*left*). The light bar denotes a 10-μm length. At right are the corresponding radial intensity profiles obtained from the patterns (*open circles*) and the analytical fit to each profile (superposed *solid curve*) found in real (video) time which was used to specify the height of the bead (*inset*) above the coverglass. (*b*) Reflection interference image of a red cell ghost before a BFP test (*left*) and the image with the BFP tip pushed into its center (*right*). The video intensity had to be amplified greatly to produce the ghost image on the left. The ghost pattern has almost disappeared at the lower gain required to view the microsphere tip at the right. As such, the fringe pattern of the probe tip was unaffected by the presence of the intervening ghost. The light bar again denotes a 10-μm distance.

As such, the integral of axial stress over the area of contact becomes proportional to the energy per area evaluated at the depth of indentation,

$$f \approx -2\pi R_S \int_{o\to\Delta z} (\partial\epsilon/\partial z)\, dz = 2\pi R_S\, \epsilon(\Delta z) \qquad (3)$$

This result is the famous Derjaguin approximation $\epsilon(\Delta z) = f/2\pi R_S$ derived originally for study of long-range interactions between a large sphere and flat substrate, which has become the hallmark of the surface forces apparatus (Israelachvili, 1992). For thicker or more dense material layers, other stresses could become significant which would necessitate a full continuum mechanical analysis of the deformation and stress fields (Hertz model, Landau and Lifshitz, 1986).

In the case of multilayer interactions, the force applied by the spherical tip represents the sum of energies/area for compression of the constituent components,

$$f/2\pi R_S \approx -\sum_n \left\{ \int_{o\to\Delta z(n)} \sigma_z\, dz_n \right\} = \sum_n \{\epsilon_n(\Delta z_n)\} \qquad (4)$$

which follows from continuity of stress, $\sigma_z = \partial\epsilon_n/\partial z_n$, between layers and the definition of total displacement, $dz \equiv \Sigma_n\, dz_n$. However, inverse relations between thickness and stress, $z_n = f_n(\sigma_z)$, for each layer are needed to determine the relative contributions Δz_n to the total indentation, $\Delta z(\sigma_z) \equiv \Sigma_n\, \Delta z_n(\sigma_z)$, which leads to a nontrivial dependence of thickness on the force gradient, $\sigma_z = -(\partial f/\partial z)/2\pi R_S$.

RESULTS AND ANALYSIS

Molecular roughness on probe tip and coverglass

Once in contact with a red cell ghost, the probe tip was separated from the coverglass by two membranes plus molecular roughnesses present on the microsphere tip and the coverglass substrate. Probe tip roughness originated from the streptavidinated PEG-biotin layer covalently linked to the glass microsphere for the purpose of attachment to the red cell force transducer. Coverglass roughness arose from the adsorption of albumin present in the buffer solution, which was needed to prevent both crenation of the red cell ghost and adhesion to glass. At the concentration of 1 mg/ml added to the buffer, albumin is known to fully cover glass surfaces with a wash-resistant coating of at least ~10^5 molecules/μm^2 (Brash and Horbett, 1987) but adsorbs little to the red cell (e.g., with bounds from ~−26 to +160 molecules/μm^2 in Janzen and Brooks, 1991). To carefully examine these roughnesses, we measured the separations of large 10-μm microspheres from coverglass substrates before and after decoration with the streptavidinated/PEG-biotin layer in 0.1 M of NaCl buffer and then in buffer plus albumin. Washed in a basic solution of ammonium hydroxide and hydrogen peroxide, clean microspheres and coverglasses exhibited negligible roughness (<~1 nm) over a lateral scale set by the wavelength of light. By comparison, streptavidinated/PEG-biotinylated microspheres were separated by ~16 ± 3 nm from the clean coverglass in buffer. But when tested in buffer plus albumin, closest approach of the streptavidinated/PEG-biotinylated microspheres to the coverglass was limited to distances of ~32 nm, which established the reference height for the thickness measurements as illustrated in Fig. 4 *c*. Thus, the ~16-nm thickness added to the streptavidin/PEG-biotin roughness seemed to arise from a tightly bound coating of albumin. However, as seen in Fig. 4, the molecular roughness in buffer plus albumin exhibited a small distance-dependent repulsion that

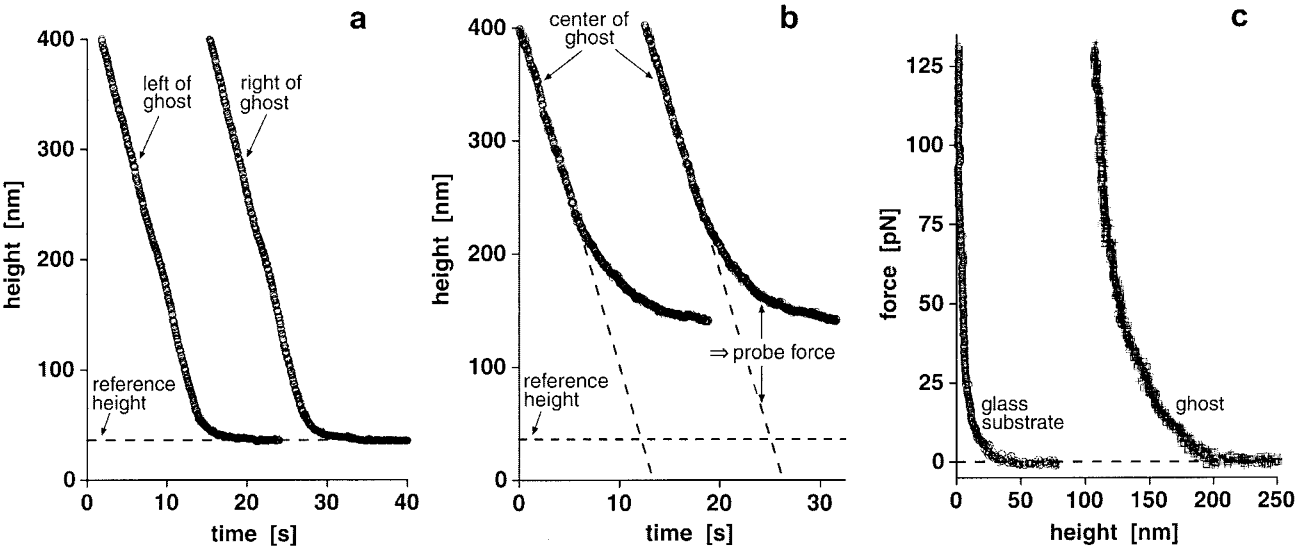

FIGURE 4 (*a*) Height of the probe tip as a function of time on approach to contact with the coverglass on either side of a ghost. (*b*) Height of the probe versus time for two approaches and indentations into the ghost center. When multiplied by the BFP *spring* constant, the deviation of the microsphere position from the piezo-driven BFP trajectory provided the measurement of probe force. (*c*) Forces of compression versus distance relative to closest approach to the coverglass as identified in (*a*).

began to resist approach much further out. This was clearly attributable to displacement of weakly adsorbed layers of albumin and had to be taken into account in the analysis of ghost membrane compression.

Thickness of two red cell membrane faces under compression by a microsphere

As demonstrated by the touch of the probe to either side of the ghost in Fig. 4 *a*, the substrate seemed to be uniform on a lateral scale of the size of the cell. When pushed twice into the ghost center, deviation of the tip movement from the probe-piezo trajectory in Fig. 4 *b* revealed the probe force versus separation relative to the reference defined by closest approach to the coverglass as shown in Fig. 4 *c*. Repeated twice in each test, identical force-distance responses showed clearly that the compliant regime was elastic and became very stiff above 70–80 pN force. Additional evidence for elastic behavior was the lack of perceptible increase in force when the speed of compression was doubled from 30 nm/s to 60 nm/s. The raw data for all the compression tests both with and without an intervening ghost are plotted in Fig. 5 as a function of net separation relative to the reference defined by closest approach to the coverglass (cf. Fig. 4 *a*). Here, the forces in each experiment have been scaled by the microsphere perimeters $2\pi R_S$ to obtain elastic energy $\epsilon(z)$ per unit area as described in the Methods section (Eqs. 2–4). After subtraction of the distance for closest approach to the coverglass, the data sets for ghost compression were superposed by small lateral shifts (±6 nm S.D.) in the origin for distance, which accounts for most of the statistical variation in thickness.

The data clustered at large distances in Fig. 5 are the total energy densities ϵ_G for compression of the ghosts. These

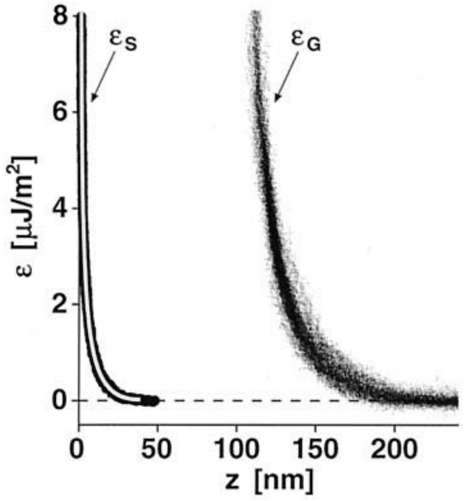

FIGURE 5 Forces scaled by the microsphere perimeters $2\pi R_S$ to give elastic energy $\epsilon(z)$ per unit area are shown for all the compression tests as a function of separation z relative to closest approach to the substrate (cf. Fig. 4 *a*). The energy densities ϵ_G clustered at large distances represent ~100 compressions of ~50 ghost double membranes. At short distances, the energy densities ϵ_S for the corresponding touches to the adjacent coverglass reveal a compliant surface roughness associated with displacement of weakly adsorbed albumin. The light curve superposed on the roughness data is the analytical approximation used to correct for the substrate compliance as described in the text.

energies per area represent superposition of energies per area for compression of two membranes $2\epsilon_M(z_M)$ plus the energy density $\epsilon_s(z_S)$ for displacement of albumin weakly adsorbed on the glass surfaces (data shown at small distances in Fig. 5), i.e.,

$$\epsilon_G(z_G) = 2\epsilon_M(z_M) + \epsilon_S(z_S) \tag{5}$$

Defined relative to the closest approach to the coverglass, z_M specifies the thickness of a single membrane, z_S is the thickness of the displaceable albumin layers, and $z_G = 2\,z_M + z_S$ is the total thickness. The relative contributions to energy density and total thickness from each component are established by stress continuity between the component layers. Thus, in principle, the energy per area for membrane compression $\epsilon_M(z_M)$ could be determined directly from Eq. 5 if the energy densities, $\epsilon_G(z_G)$ and $\epsilon_s(z_S)$, plotted in Fig. 5 were evaluated at thickness values, z_G and z_S, where the slopes, $\partial\epsilon_G/\partial z_G$ and $\partial\epsilon_S/\partial z_S$, are equal. The difficulty arises in evaluation of derivatives at discrete datapoints modulated by experimental noise. Obviously, analytical functions which smoothly approximate the data and average out the noise are needed to carry out this decomposition.

Substrate roughness

To begin, the energy densities measured for contact to the adjacent glass surfaces were fit with a simple phenomenological expression that satisfied the mechanical requirements of zero stress ($\partial\epsilon_S/\partial z_S = 0$) and zero energy density ($\epsilon_S = 0$) at an outer material boundary ($z_S = h_S$). The simplest approach was to use the sum of an inverse power law plus an ascending-linear term,

$$\epsilon_S(x_S) = c_S\{x_S + 1/(qx_s^q) - 1 - 1/q\} \tag{6}$$

where dimensionless thickness ($1 \geq x_S \geq 0$) is defined by $x_S \equiv z_S/h_S$. The scale for energy density is embodied in the prefactor c_S (μJ/m^2). The dependence of stress on thickness is given by $\sigma_z = \partial\epsilon_S/\partial z_S = (c_S/h_S)\ \{1 - 1/x_S{}^{q+1}\}$, which is inverted easily to specify the dependence of thickness on stress, $z_S = h_S/\{1 - h_S\sigma_z/c_S\}^{1/q+1}$. Shown by the curve superposed on the data in Fig. 5, the energies per area for displacement of weakly adsorbed albumin were well fit by the expression $\epsilon_S(x_S) \approx c_S\ \{x_S + 1.724/x_S{}^{0.58} - 2.724\}$ with $c_S \approx 0.657\ \mu\text{J/m}^2$ and $h_S \approx 39$ nm.

Elastic model of membrane compressibility

In modeling the compliance of the red cell membrane, we have assumed that 1) only the spectrin network is compressible and 2) spectrin tetramers behave like ideal flexible polymers defined by a known contour length L (≈ 200 nm) and an unknown statistical segment length b. At the simplest level, a low-density network formed by flexible polymers is predicted to stiffen as an inverse-square law under compression, i.e., $\epsilon_N \sim c_N(h_N/z_N)^2$ for $z_N \to 0$ based on a free chain end-to-end length given by $h_N \approx (Lb)^{1/2}$. Most importantly, the scale for energy density c_N is set by the number of chains per area ρ and room temperature thermal energy k_BT ($\sim 4 \times 10^{-21}$ J), i.e., $c_N = \rho k_BT$. Given a density of $\rho \approx 700/\mu\text{m}^2$ for spectrin tetramers in the network, we expect that an energy density of $c_N \approx 2.8\ \mu\text{J/m}^2$ should govern network compliance. However, when doubled to represent two membranes and compared with the data plotted in Fig. 5, we see immediately that the energy density only reaches $\sim k_BT$ per spectrin tetramer near maximum compression in the experiments. Moreover, with the energy density scale set at $c_N = 2.8\ \mu\text{J/m}^2$, the inverse square law for compression requires unrealistically low values of h_N (≈ 10 nm) to follow the rapid decrease in energy density from maximum compression, and remains above the measurements at large distances. Thus, we conclude that the soft-compliant regime of thickness from ~50 nm to ~90 nm per membrane represents elastic compression of the outer loop region of spectrin and could involve other long-range repulsive interactions.

To model the elastic compliance of spectrin loops, we have assumed that the spectrin chains are dilute (estimated mass density of ~3 mg/ml for a ~50-nm thick layer) and can therefore invoke the random-walk theory introduced by Edwards many years ago to predict repulsion by a single polymer tethered to a solid surface (Edwards and Freed, 1969; Dolan and Edwards, 1974). Summarized in Appendix II, the random flight analysis predicts the number $\Omega(L', h)$ of configurations accessible to a loop attached to one surface when confined by the presence of another surface at a distance h, relative to the unconfined loop when $h \to \infty$. [Noted in Appendix II, L' is an effective contour length for the one-dimensional abstraction, which stems from the geometric limit to chain extension, $L' = (L^2 - d^2)^{1/2}$, set by the distance d between the ends of the loop. For spectrin tetramers in situ, $d \approx 70$ nm implies that $L' \approx 187$ nm.] With the reduction in entropy predicted by $k_B\ \log_e[\Omega(L', h)]$ through Eqs. AII-5 and AII-6 of Appendix II, the elastic energy density $\{-\rho k_BT \log_e[\Omega(L', h)]\}$ of a network formed by dilute polymer loops is modeled by the following approximation:

$$\epsilon_N(x_N) \approx \rho k_BT[1.645/x_N^2 + 3\log_e(x_N) - 1.56] \tag{7}$$

when $x_N < 0.8$ and,

$$\epsilon_N(x_N) \approx \rho k_BT\{(24x_N^2 - 2)\exp[-6x_N^2]\} \tag{8}$$

when $x_N > 0.8$. The dimensionless thickness $x_N = z_N/h_N$ is scaled by the free end-to-end length $h_N = (L'b)^{1/2}$ of an unattached chain. As shown in Fig. AII-1 in Appendix II, the ideal loop model for network elasticity approaches the expected inverse square law dependence on thickness only when compressed well below the free chain end-to-end

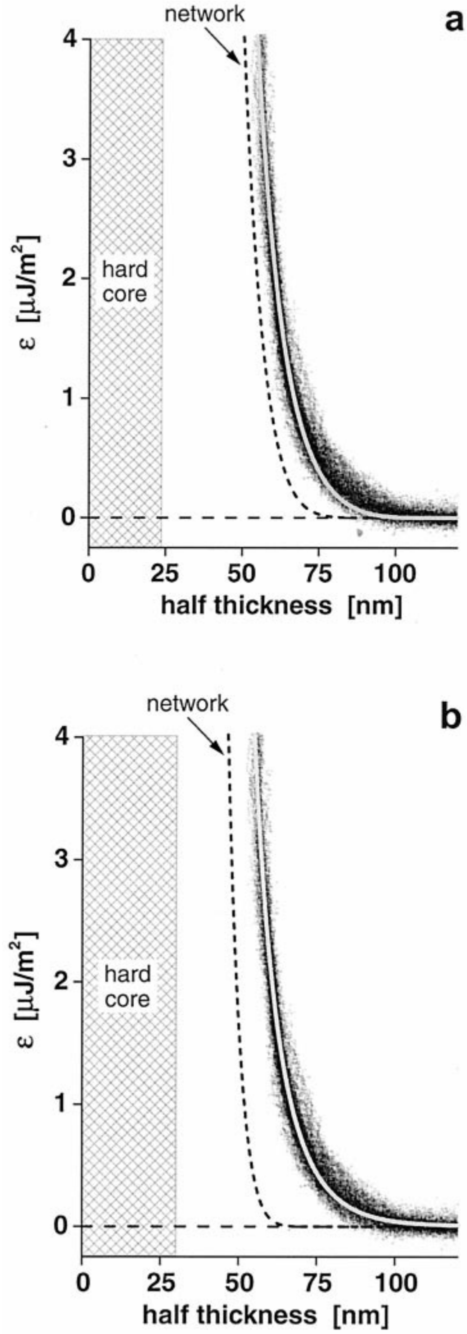

FIGURE 6 Correlations of the models for membrane thickness elasticity plus roughness compressibility to the measurements of energy density and thickness in ghost tests. For these comparisons, the data for both total energy density and thickness seen in Fig. 5 have been divided by two to reflect partition between the two membranes of the ghost. (*a*) Direct fit of the model for an elastic network of dilute spectrin loops neglecting other long-range interactions (*light curve* superposed on the data). The network elastic response predicted by the fit (*dashed curve*) is characterized by a free chain end-to-end length of ~45 nm (i.e., statistical segment length of ~11 nm) and starts from a hardcore limit at ~24 nm (*cross-hatched area*). (*b*) Fit of the elastic network model including long-range repulsion because of confinement of membrane thermal-bending excitations (*light curve* superposed on the data). A much better match to the data at large distances, the correlation here predicts that the network (*dashed curve*) is characterized by a free chain end-to-end length of ~29 nm (i.e., statistical segment length of ~5 nm) and starts from a hardcore limit at ~30 nm (*cross-hatched area*).

length defined by h_N and exhibits a soft Gaussian-like decay under weak compression.

To correlate the elastic network model with the data in Fig. 5, it was necessary to satisfy the condition of stress continuity between each membrane network and the displaceable albumin roughness, i.e., $\sigma_Z = \partial\epsilon_N/\partial z_N = \partial\epsilon_S/\partial z_S$. The requirement of stress continuity led to parameterization of all thicknesses and energy densities in terms of the dimensionless network thickness x_N. For instance, the derivative of the roughness energy density was inverted to express thickness in terms of stress, i.e.,

$$z_S = h_S/[1 - \sigma_z(x_N)\, h_S/c_S]^{1/1.58}$$

and stress was defined by the derivative of network energy density based on Eqs. 7, 8, i.e.,

$$\sigma_z(X_N) \approx -(\rho k_B T/h_N)\,[3.29/x_N^3 - 3/x_N] \qquad (9)$$

when $x_N < 0.8$ and,

$$\sigma_z(x_N) \approx -48\,(\rho k_B T/h_N)\,\{(6x_N^3 - x_N)\exp[-6x_N^2]\} \qquad (10)$$

when $x_N > 0.8$. In this way, the energy density scale for the spectrin network could be set at k_BT/chain ($\rho k_B T = 2.8$ μJ/m^2) and then the total energy density, $\epsilon_G(z_G) = 2\epsilon_N(x_N) + \epsilon_s(z_S)$, will fit to the ghost measurements as a function of total distance $z_G = 2\,(z_B + h_N x_N) + z_S$. Optimization of the fit was performed through variation of h_N and the constant z_B added to account for a hardcore limit to compression. Neglecting other interactions, direct correlation of the loop model to the data yielded values of $h_N \approx 45$ nm and $z_B \approx 24$ nm; the fit is shown by the curve superposed on the data in Fig. 6 *a*. Thus, the direct fit resulted in a value of $b \approx 11$ nm for the statistical segment length of spectrin. [Note, for comparison to the elastic response of the network, the data for both total energy density and thickness have been divided by two in Fig. 6 to reflect partition between the two membranes of the ghost.]

Membrane compressibility plus thermal undulations

Although the fit to the data shown in Fig. 6 *a* looks reasonable, it falls significantly below the measured elastic response at large distances. Thus, we considered the possibility that other interactions may also contribute to elastic compliance at large separations. First, the major source for electrostatic repulsion, which arises from the highly charged inner leaflets of the bilayer, could be ruled out because the interaction decays exponentially with ~1 nm decay length in 0.1 M of salt and would be negligible at separations on the scale of 100 nm. Thus, the most likely contribution to repulsion at large distances seemed to be confinement of membrane thermal undulations as discovered originally by Helfrich (1978; Helfrich and Servuss, 1984). Ubiquitous, the subtle entropy-driven effect is always present when stretching or pushing on biomembranes because of their exceptional flexibility. Following Helfrich, we modeled the steric repulsion because of confinement of membrane undulations by an inverse distance-squared interaction,

$$\epsilon_{\mathrm{Fl}} = e_{\mathrm{H}}/z_{\mathrm{Fl}}^2 \tag{11}$$

where z_{Fl} defines the distance available for random out-of-plane displacements. The Helfrich energy scale, $e_{\mathrm{H}} \approx (k_{\mathrm{B}}T)^2/16\pi^2 k_{\mathrm{c}}c$, is governed by the membrane bending modulus k_{c}, thermal energy, and a constant $c \approx 0.1$ for Gaussian-distributed amplitudes of bending modes (Evans, 1991). The red cell membrane bending stiffness is dominated by the lipid bilayer (Mohandas and Evans, 1994); so we have taken the membrane bending stiffness to be $k_{\mathrm{c}} \sim 25\text{–}30\ k_{\mathrm{B}}T$, which yields a value of $e_{\mathrm{H}} \approx 10^{-23}$ J for the Helfrich energy scale per membrane. The scale e_{H} becomes 10 μJ/m^2 in energy density when the distance z_{Fl} is normalized by 1 nm. In this way, the total energy density in ghost compression was augmented to include the long-range steric interaction for two membranes, $\epsilon_{\mathrm{G}}(z_{\mathrm{G}}) = 2\ [\epsilon_{\mathrm{N}}(x_{\mathrm{N}}) + \epsilon_{\mathrm{Fl}}(z_{\mathrm{Fl}})] + \epsilon_{\mathrm{s}}(z_{\mathrm{S}})$. The long-range steric interaction must satisfy stress continuity, and the space available for membrane undulations is thereby parameterized by network thickness, i.e., $z_{\mathrm{Fl}} = [-2e_{\mathrm{H}}/\sigma_{\mathrm{Z}}(x_{\mathrm{N}})]^{1/3}$. With the total thickness now given by $z_{\mathrm{G}} = 2\ (h_{\mathrm{N}}x_{\mathrm{N}} + z_{\mathrm{Fl}} + z_{\mathrm{B}}) + z_{\mathrm{S}}$ and the network energy scale set to $k_{\mathrm{B}}T$/chain, the model of a polymer network riding on thermal undulations was matched to the data. Superposed on the data in Fig. 6 *b*, the fit was much improved at large separations (vis a vis Fig. 6 *a*) by inclusion of the membrane steric interaction. Concomitantly, there was a significant reduction in the spectrin free end-to-end length ($h_{\mathrm{N}} \approx 29$ nm) and statistical segment length ($b \approx 5$ nm). The apparent core thickness was increased slightly to $z_{\mathrm{B}} \approx 30$ nm.

CONCLUSIONS AND DISCUSSION

The thickness of the red cell membrane was found to respond elastically to compression with a surprisingly soft compliance that began at very large distances. Relative to closest approach on the glass substrate, the probe first sensed the presence of red cell structure at an apparent thickness of ~90 nm per membrane under impingement forces of ~1 pN, but then stiffened significantly on approach to ~50 nm per membrane under impingement forces of ~100 pN, which corresponded to stresses of only ~10^{-3} atm. Although initially puzzling, this was not the first time that red cell membrane thicknesses of this magnitude had been observed. Similar values were found in the electron microscopy studies of Bull et al. (1986). Examining red cells which had been flow-deformed into *saddlebag* shapes around spider webs, these researchers obtained thicknesses of ~57 nm per membrane in the thin isthmus zone adjacent to the web fiber. But when the *saddlebag* shapes were lysed before fixation, the membrane thickness in the isthmus zone expanded to a dimension of ~107 nm per membrane. In addition, Bull et al. again obtained low values of ~61 nm per membrane in the thin dimple region when red cells were osmotically dehydrated and then heat-denatured at 49.5°C to form membrane-to-membrane cross-bridges. Clearly, both maximum and minimum thicknesses from Bull et al. (1986) are consistent with the apparent thicknesses of unfixed red cell membranes in our probe tests. In another report, Fischer (1988) used electron microscopy to examine the dimple regions of red cells which had been chemically cross-bonded by diamide (N-ethylmaleimide) or ATP depletion and by denaturation at 46°C or by urea. Carried out under conditions of high osmotic stress (~600 mOsm), Fischer obtained much smaller, but more broadly distributed, thicknesses from 20 to 60 nm per membrane. Likely caused by the strong osmotic dehydration in combination with protein aggregation, these small thicknesses are consistent with the range between the hardcore dimension derived from the correlations in Fig. 6 and the thickness per membrane obtained at maximum probe force in our experiments.

Fully recoverable after indentation, the soft elastic regime of red cell membrane compressibility exhibited a deceptively simple dependence on distance, which we have correlated with a model network composed of random-flight polymer loops. In the idealized one-dimensional abstraction used here, the elastic response to compression begins at large separations with a weak Gaussian-like rise in energy but then stiffens to an inverse square dependence on thickness near the polymer radius of gyration $(Lb/6)^{1/2}$ or compact thickness of the network. When fit directly to the measurements of energy density (corrected for displacement of albumin weakly adsorbed to the glass substrates), the model of the red cell membrane yields a free chain end-to-end length $(Lb)^{1/2}$ for spectrin of ~45 nm and a statistical segment length of $b \sim 11$ nm. The direct fit predicts that the network is backed by a molecular hardcore thickness of ~24 nm, which is comparable with the estimates given in the introduction based on structural analysis. However, although the outer loop region extends network compliance beyond the free chain end-to-end length, the direct fit falls below the very soft resistance to compression sensed at large distances in the experiments. In contrast, the full range of compliance seems to be well fit by the elastic network model when we include the long-range steric repulsion that arises from confinement of membrane thermal-bending excitations. In this case, spectrin and the network thickness are found to be characterized by a smaller free chain end-to-end length of ~29 nm and statistical segment length of $b \sim 5$

nm. The hardcore dimension increased slightly to ~30 nm. Inherent to highly flexible interfaces, collective bending excitations are known to play a major role in biomembrane elastic properties such as area elasticity (Evans and Rawicz, 1990, 1997; Rawicz et al., 2000) and in interactions between membranes (Evans and Parsegian, 1986; Lipowsky and Leibler, 1986; Evans, 1991), which shows up here as ~20% increase in apparent thickness of the red cell membrane.

Correlation of the network modeled as ideal polymer loops to our probe measurements has led to the statistical picture of spectrin as a freely jointed chain of 20–40 segments with lengths that correspond to ~1–2 times the 5 nm triple α-helical domains in spectrin (Grum et al., 1999). This freely jointed chain is similar to, but somewhat more flexible than, the worm-like chain represented by a persistence length of ~10 nm in studies of detergent-extracted red cell cytoskeletons (Svoboda et al., 1992) and isolated spectrin (Stokke et al., 1986). Turning to simulations of spectrin chains modeled as a series of beads constrained by string-like tethers, Boal (1994) and Discher et al. (1998) have explored network properties with chains that range in number of segments from 4 to 30 where segment length b was ~1.2 times the bead diameter a (i.e., $b \approx 1.2\ a$). Although direct comparison to our experiments is difficult because the networks were not under compression, Boal (1994) and Discher et al. (1998) did derive first and second moments of the segment distribution in the thickness dimension. The first moment was the mean or mass-average thickness $\langle z \rangle$, which is stated to be approximately half the effective geometric thickness (Discher et al., 1998). For example, when modeled by ~26 segments in a contour length of 200 nm, the simulations yielded a mean thickness for the spectrin network of ~15 nm, which would imply an effective thickness (~30 nm) not that different from our results (when thermal-bending fluctuations were taken into account). Even so, there are important differences between the idealized model of polymer loops as random flight chains and simulations based on chains modeled as a necklace of beads. Described in Appendix II, the mean-mass thickness of the network in the random flight approximation is given by, $\langle z \rangle / b = 0.36\ (L/b)^{1/2}$. By comparison, the mean thickness in the simulations depended more strongly on number of beads per chain, first as $\langle z \rangle / b \approx 0.1\ (L/b)$ for $L/b < 17$ then as $\langle z \rangle / b \approx 0.19\ (L/b)^{0.7}$ for $17 < L/b < 25$, and presumably as $\sim (L/b)^{0.6}$ for very large values of L/b (Boal, 1994). Next, calculating first and second moments of thickness in the simulations, fluctuations in mean thickness were used by Boal and Discher et al. to derive a transverse modulus $Y_\perp$ through the relation, $Y_\perp = (\rho k_B T)\ \{\langle z \rangle / [\langle z^2 \rangle - \langle z \rangle^2]\}$. In the random flight approximation, this transverse-fluctuation modulus is predicted by, $Y_\perp \approx 10\ (\rho k_B T/b)\ (b/L)^{1/2}$, and matches the network stiffness at a compression of x_N ~0.8–0.9. Based on correlations of the random flight theory shown in Fig. 6, a and b, the transverse moduli would be 600 and 880 mN/m^2, respectively. By comparison, the transverse moduli in the simulations of Boal (1994) were found to scale as $Y_\perp \approx 64\ (\rho k_B T/b)\ (b/L)^{3/4}$, and predicted a value of ~2000 mN/m^2 for the red cell cytoskeleton, which is 2–3–fold stiffer. In contrast, the transverse moduli in simulations of condensed and prestressed networks (Discher et al., 1998) imply values 5–10–fold still greater than the unstressed simulation. However, it is important to recognize that harmonic measures based on fluctuations in mean thickness cannot capture the anharmonic response inherent in the mechanical stiffness of the cytoskeleton.

APPENDIX I: Analysis of Newton-ring interference pattern

To form a Newton-ring pattern by reflection interference microscopy, the components of light reflected from the coverglass-buffer interface and the underside of the microsphere must be mutually coherent and collected by the objective. The principal difficulty is that the illumination is spatially incoherent and only temporally coherent over a short distance. So, to be imaged by the objective, the interference pattern must exist at the object focus location. In terms of geometrical optics, only the mutually coherent rays of reflected light that *cross* in the object region contribute to the interference pattern imaged by the objective. The ray crossings create a three-dimensional interference pattern local to the object. For a high NA objective with very small depth of focus, a two-dimensional "slice" of this three-dimensional pattern is visualized in image space. Thus, a Newton-ring pattern and, thereby, the apparent sphere-substrate distance depend on the object plane of focus. Usually, an observer will adjust the focus to produce an interference pattern with the best contrast. However, the position of this observational plane changes with the separation between sphere and coverglass, which compromises height measurements. Therefore, to avoid the difficulties associated with a variable focal plane, the measurements in this study were performed with the microscope focused at the coverslip-buffer interface.

In our analysis, we have used geometrical optics to model interference of reflected light at the coverglass-buffer interface. Because monochromatic Hg illumination is only temporally coherent, the reflected rays must originate from common incoming rays which leads to a unique mapping between incoming rays and the loci of interference. In Fig. AI-1 we see that the interference pattern at the coverslip-buffer interface is generated exclusively by rays which reflect from the microsphere under normal incidence. Based on the optical path difference,

$$\Lambda(r) = 2\ n_2 \{[r^2 + (h + R_S)^2]^{1/2} - R_S \qquad \text{(AI-1)}$$

the phase difference is given by

$$\Delta(r) = 2\pi\Lambda(r)/\lambda_o + \delta$$
$$= 4\pi n_2\{[r^2 + (h + R_S)^2]^{1/2} - R_S\}/\lambda_o + \pi \quad \text{(AI-2)}$$

where r is the radial distance from the axis of symmetry; R_S is the microsphere radius; and h is height of the microsphere above the coverglass. The value of refractive index was $n_2 \cong 1.34$ for the buffer solution and the wavelength was $\lambda_o = 546.1$ nm in the experiments. A phase shift of $\delta = \pi$ is introduced to account for the reflection at the high index glass surface of the microsphere. Extrema of the cosine of the phase shift $\Delta(r)$ determine the positions of fringes in the Newton-ring pattern. Much less tractable, the pattern is modulated by the angle-dependence of reflected intensity through Fresnel coefficients, which is convolved with the diffraction-limited transfer function of the microscope. As described previously by Radler and Sackmann (1992), the practical approach is to superpose Gaussian contrast functions on the ideal radial intensity profile,

$$I(r) = A_1 \exp(-b_1 r^2) + A_2 \exp(-b_2 r^2) \cos[\Delta(r)] \quad \text{(AI-3)}$$

where $A_{1,2}$ and $b_{1,2}$ are empirical fitting parameters. Eq. AI-3 is the intensity function used to extract height above the coverglass from the radial fringe patterns created by microspheres in our experiments.

APPENDIX II: Entropic confinement of a polymer loop

We briefly summarize the well known random flight theory for a single polymer chain attached to a surface (Edwards and Freed, 1969; Dolan and Edwards, 1974) and apply the theory to a polymer loop. The key element in the theory is the probability distribution $G(r, r', s)$ which is used to describe the number of s-length configurations that start from one end of the chain at position r and end at r'. This distribution is predicted by solution to a diffusion equation where time is replaced by the number s/b of random steps and a diffusivity proportional to the square step size, e.g., $b^2/6$ in three dimensions. For confinement by a second surface placed at distance h, two equivalent series expansions are given by Dolan and Edwards (1974) for the component of the probability distribution perpendicular to a surface: i.e., one that converges rapidly at small separation,

$$G(z, z', s, h) = (2/h) \sum_{n=1\to\infty} \sin(n\pi z/h) \sin(n\pi z'/h)$$
$$\times \exp[-(Lb)\pi^2 n^2/6h^2] \quad \text{(AII-1)}$$

and another that converges at large separations

$$G(z, z', s, h) = (3/2\pi Lb)^{1/2}$$
$$\sum_{-\infty<m<\infty} \{\exp[-3(z - z' - 2mh)^2/2Lb]$$
$$- \exp[-3(z + z' - 2mh)^2/2Lb]\} \quad \text{(AII-2)}$$

where z, z' are positions along the normal to the tethering surface. As applied originally to the case of a polymer tethered at only one end to a surface, the random walk must be started at a small distance δ_b from the surface (conceptualized as the end of the first chain segment), which introduces a δ_b-dependent scale factor in the probability distribution. If we assume that the distance d between ends on the tethering surface is short compared with the contour length, the one-dimensional approach can be applied similarly to the case of loops. The effective contour length L' for the one-dimensional abstraction is defined by the geometric limit to chain extension, $L' = (L^2 - d^2)^{1/2}$, which for spectrin chains tethered at 70 nm distances differs by less than 10% from the bare contour length of $L = 200$ nm. As such, the distributions in Eqs. AII-1, 2 are used to specify the relative number of random walks for L'/b steps within the confined separation that start and end at distance δ_b,

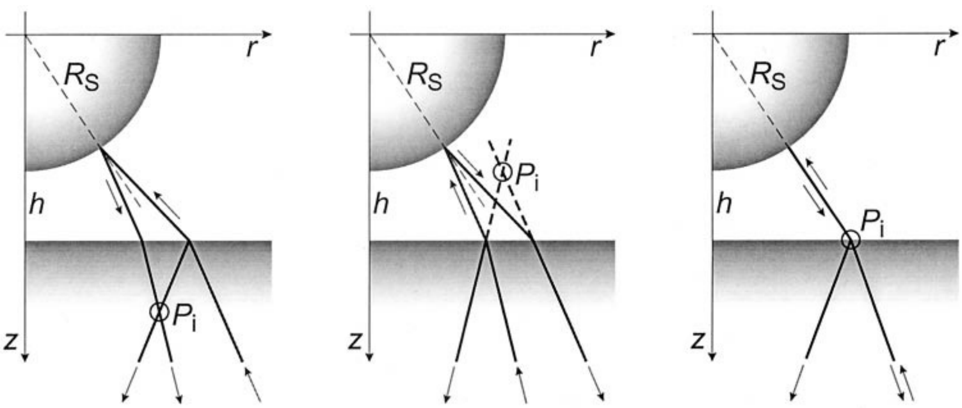

AI-1. Locations of self-interference for rays of light reflected from the underside of a microsphere and from the coverglass-buffer interface, which would be imaged at different focus positions P_i.

$$G(\delta_b, \delta_b, L', h) = (2/h) \sum_{n=1\to\infty} \sin^2(n\pi\delta_b/h) \times \exp[-(L'b)\pi^2 n^2/6h^2] \quad \text{(AII-3)}$$

for small separations and

$$G(\delta_b, \delta_b, L', h) = (3/2\pi L'b)^{1/2} \sum_{-\infty<m<\infty} \{\exp[-6m^2h^2/L'b] - \exp[-6(mh - \delta_b)^2/L'b]\} \quad \text{(AII-4)}$$

at large separations. Finally, the number of configurations $\Omega(L', h)$ for confined loops relative to the number of configurations for unconfined loops at infinite separation is derived from the ratio $G(\delta_b,\delta_b,L', h)/G(\delta_b,\delta_b,L',\infty)$ in the limit that $\delta_b \to 0$. The outcome is closely approximated by the ratio of lead terms in each series expanded to quadratic order in δ_b,

$$\Omega(L', x) \approx (\pi/6)^{1/2}\,(2\pi^2/3x^3)\exp[-\pi^2/6x^2] \quad \text{(AII-5)}$$

for small, dimensionless separations $x = h/(L'b)^{1/2} < {\sim}0.8$ and

$$\Omega(L', h) = 1 + 2(1 - 12x^2)\exp[-6x^2] \quad \text{(AII-6)}$$

for large separations $h/(L'b)^{1/2} > {\sim}0.8$. Using the entropy reduction predicted by $k_B \log_e[\Omega(L', h)]$, we obtain the following approximation for free energy density of compression given a network formed by dilute polymer loops,

$$\varepsilon(x) \approx \rho k_B T\,[\pi^2/6x^2 + 3\log_e(x) - \tfrac{1}{2}\log_e(2\pi^5/27)] \quad \text{(AII-7)}$$

when $x < 0.8$ and

$$\varepsilon(x) \approx -\rho k_B T\,\{\log_e[1 - (24x^2 - 2)\exp[-6x^2]]\} \quad \text{(AII-8)}$$

when $x > 0.8$. The elastic energy per loop is plotted in Fig. AII-1 along with the Dolan and Edwards result for a polymer tethered at one end to a surface as a comparison. We see that the energy density of the network approaches the expected inverse square law dependence on thickness when compressed well below the free end-to-end length of an unattached chain defined by $(Lb)^{1/2}$ but crosses over to a Gaussian-dominated regime that diminishes rapidly as thickness exceeds $(Lb)^{1/2}$.

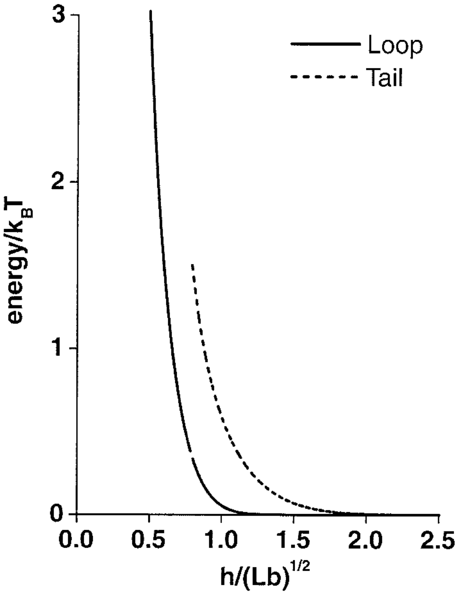

AII-1. Random-flight approximation in one dimension for the free energy of a loop as a function of the confinement distance (*solid curve*). The scale is defined by free end-to-end length $(Lb)^{1/2}$ of an unattached chain and the break in the curve marks the cross-over between the inner/outer solutions (Eqs. AII-7,8). Also, plotted is the result from Dolan and Edwards (1974) for the tail of a polymer tethered at only one end. Both energies approach an inverse square law dependence on thickness when compressed well below the free chain end-to-end length but exhibit a Gaussian-dominated regime that diminishes rapidly as thickness exceeds $(Lb)^{1/2}$.

A useful corollary to the properties of a confined loop is the probability distribution for segment density in an unconfined loop. This is found from the joint probability for the number of random walks of s steps from one tethered end and walks of the complementary $L' - s$ steps from the opposite tethered end that meet at z, which is then integrated over the range of s to specify the probability density for all walks, i.e., $p(z) = \int_{o<s<L} G(\delta_b, z, s, \infty)\, G(z, \delta_b, L' - s, \infty)\, ds$. The result is a Rayleigh distribution,

$$p(z) = 12\,(z/L'b)\exp(-6z^2/L'b) \quad \text{(AII-9)}$$

Thus, thickness moments of a loop in the one-dimensional approximation are given by

$$\begin{aligned} \langle z^n\rangle &= Lb/6)^{n/2}\, n!!\,(\pi/2^{n+1})^{1/2} && \text{for odd } n \\ \langle z^n\rangle &= (Lb/6)^{n/2}\,(n/2)! && \text{for even } n \end{aligned} \quad \text{(AII-10)}$$

where $(Lb/6)^{1/2}$ is the radius of gyration or correlation length for a random walk.

We gratefully acknowledge the expert technical assistance of Andrew Leung at the University of British Columbia. The work was supported by grant HL31579 from the National Institutes of Health.

REFERENCES

Bennett, V. 1990. Spectrin based membrane skeleton–a multipotential adapter between plasma membrane and cytoplasm. *Physiol. Rev.* 70: 1029–1060.

Boal, D. H. 1994. Computer simulation of a model network for the erythrocyte cytoskeleton. *Biophys. J.* 67:521–529.

Brash, J., and T. Horbett, editors. 1987. Proteins at Interfaces. No. 343. American Chemical Society, Washington, D.C.

Bull, B. S., Weinstein, R. S., and R. A. Korpman. 1986. On the thickness of the red cell membrane skeleton: quantitative electron microscopy of maximally narrowed isthmus regions of intact cells. *Blood Cells.* 12: 25–42.

Byers, T. J., and D. Branton. 1985. Visualization of the protein associations in the erythrocyte membrane skeleton. *Proc. Natl. Acad. Sci. U.S.A.* 82:6153–6157.

Cohen, C. M. 1983. The molecular organization of the red cell membrane skeleton. *Semin. Hematol.* 20:141–158.

Discher, D. E., D. H. Boal, and S. K. Boey. 1998. Simulations of the erythrocyte cytoskeleton at large deformation. II. Micropipette aspiration. *Biophys. J.* 75:1584–1597.

Dolan, A. K., and S. F. Edwards. 1974. Theory of the stabilization of colloids by adsorbed polymer. *Proc. R. Soc. Lond. A.* 337:509–516.

Edwards, S. F., and K. F. Freed. 1969. The entropy of a confined polymer: I. *J. Phys. A.* 2:145–150.

Evans, E. 1991. Entropy-driven tension in vesicle membranes and unbinding of adherent vesicles. *Langmuir.* 7:1900–1908.

Evans, E. A., and V. A. Parsegian. 1986. Thermal-mechanical fluctuations enhance repulsion between bimolecular layers. *Proc. Natl. Acad. Sci. U.S.A.* 83:7132–7136.

Evans, E., and W. Rawicz. 1990. Entropy-driven tension and bending elasticity in condensed-fluid membranes. *Phys. Rev. Lett.* 64: 2094–2097.

Evans, E., and W. Rawicz. 1997. Elasticity of *fuzzy* biomembranes. *Phys. Rev. Lett.* 79:2379–2382.

Evans, E., K. Ritchie, and R. Merkel. 1995. Sensitive force technique to probe molecular adhesion and structural linkages at biological interfaces. *Biophys. J.* 68:2580–2587.

Fischer, T. 1988. Role of spectrin in cross bonding of the red cell membrane. *Blood Cells.* 13:377–394.

Grum, V. L., D. Li, R. I. MacDonald, and A. Mondragon. 1999. Structures of two repeats of spectrin suggest models of flexibility. *Cell.* 98: 523–535.

Helfrich, W. 1978. Steric interaction of fluid membranes in multilayer systems. *Z. Naturforsch.* 33a:305–315.

Helfrich, W., and R. M. Servuss. 1984. Undulations, steric interaction, and cohesion of fluid membranes. *Nuovo Cimento.* D3:137–151.

Israelachvili, J. N. 1992. Intermolecular and Surface Forces. Academic Press, San Diego.

Janzen, J., and D. E. Brooks. 1991. A critical reevaluation of the "nonspecific" adsorption of plasma proteins and dextrans to erythrocytes and the role of these in rouleaux formation. *In* Interfacial Phenomena in Biological Systems, Vol. 39: Surfactant Science Series. Max Bender, editor. Marcel Dekker, New York. 193–247.

Landau, L. D., and E. M. Lifshitz. 1986. Theory of Elasticity, 3rd ed. Pergamon Press, Tarrytown, NY.

Levine, S., M. Levine, K. A. Sharp, and D. E. Brooks. 1983. Theory of electrokinetic behavior of human erythrocytes. *Biophys. J.* 42:127–135.

Linss, W., Pilgrim, C., and H. Feuerstein. 1991. How thick is the glycocalyx of human erythrocytes [in German]. *Acta Histochem.* 91:101–104.

Lipowsky, R., and S. Leibler. 1986. Unbinding transitions of interacting membranes. *Phys. Rev. Lett.* 56:2541–2544.

McGough, A. M., and R. Josephs. 1990. On the structure of erythrocyte spectrin in partially expanded membrane skeletons. *Proc. Natl. Acad. Sci. U.S.A.* 87:5208–5212.

Mohandas, N., and E. Evans. 1994. Mechanical properties of the red cell membrane in relation to molecular structure and genetic defects. *Annu. Rev. Biophys. Biomol. Struct.* 23:787–818.

Picart, C., and D. E. Discher. 1999. Actin protofilament orientation at the erythrocyte membrane. *Biophys. J.* 77:865–878.

Radler, J., and E. Sackmann. 1992. On the measurement of weak repulsive and frictional colloidal forces by reflection interference contrast microscopy. *Langmuir.* 8:848–853.

Rawicz, W., K. Olbrich, T. McIntosh, D. Needham, and E. Evans. 2000. Effect of chain length and unsaturation on elasticity of lipid bilayers. *Biophys. J.* 79:328–339.

Stokke, B. T., A. Mikkelsen, and A. Elgsaeter. 1986. Spectrin, human erythrocyte shapes, and mechanochemical properties. *Biophys. J.* 49: 319–327.

Svoboda, K., C. F. Schmidt, D. Branton, and S. M. Block. 1992. Conformation and elasticity of the isolated red cell membrane skeleton. *Biophys. J.* 63:784–793.

Wiegand, G., K. R. Neumaier, and E. Sackmann. 1998. Microinterferometry: three-dimensional reconstruction of surface microtopography for thin-film and wetting studies by reflection interference contrast microscopy (RICM). *Applied Optics*. 37:6892–6905.

Zilker, A., M. Ziegler, and E. Sackmann. 1992. Spectral analysis of erythrocyte flickering in the 0.3–4-μm^{-1} regime by microinterferometry combined with fast image processing. *Phys. Rev. A.* 46:7998–8001.